

Analog of a quantum heat engine using a single-spin qubit

K. Ono^{1,2*}, S. N. Shevchenko^{3,4,5†}, T. Mori⁶, S. Moriyama⁷, Franco Nori^{5,8}

¹Advanced device laboratory, RIKEN, Wako-shi, Saitama 351-0198, Japan

²CEMS, RIKEN, Wako-shi, Saitama 351-0198, Japan

³B. Verkin Institute for Low Temperature Physics and Engineering, Kharkov 61103, Ukraine

⁴V. N. Karazin Kharkiv National University, Kharkov 61022, Ukraine

⁵Theoretical Quantum Physics Laboratory, Cluster for Pioneering Research, RIKEN, Wako-shi, Saitama 351-0198, Japan

⁶Device Technology Research Institute (D-Tech), National Institute of Advanced Industrial Science and Technology (AIST), Tsukuba, Ibaraki 305-8568, Japan

⁷Department of Electrical and Electronic Engineering,

Tokyo Denki University, Adachi-ku, Tokyo 120-8551, Japan and

⁸Department of Physics, The University of Michigan, Ann Arbor, MI 48109-1040, USA

A quantum two-level system with periodically modulated energy splitting could provide a minimal universal quantum heat machine. We present the experimental realization and the theoretical description of such a two-level system as an impurity electron spin in a silicon tunnel field-effect transistor. In the incoherent regime, the system can behave analogously to either an Otto heat engine or a refrigerator. The coherent regime could be described as a superposition of those two regimes, producing specific interference fringes in the observed source-drain current.

Introduction.— Thermodynamics was originally developed for classical many-particles systems, but recently it is being applied for the description of individual quantum systems. This emergent field is known as Quantum Thermodynamics [1]. In several review articles different types of quantum heat engines were considered, e.g. Refs. [2–6].

What essentially distinguishes a working medium of a quantum heat engine from a classical one is the ability to be in a coherent superposition of its states [7, 8]. In this way, the study of superpositional interference phenomena in prototypical quantum heat engines is important, since this can provide a quantum advantage in their performance, meaning the ability of a quantum heat engine to produce more power than an equivalent classical heat engine [8, 9].

The simplest realization of a quantum heat machine would be a two-level system. Such system, with a periodically modulated energy splitting, could work as either a heat engine or a refrigerator, thus providing a minimal universal quantum heat machine [10–12]. Different proposed realizations are based on either natural or artificial atoms [13], including superconducting and semiconducting circuits, e.g., Refs. [14–22]. Recently, experimental realizations of single-atom heat engines were demonstrated with trapped ions [23–25] and nitrogen-vacancy centers in diamond [8]. In this work we present an experimental realization and a theoretical description of heat-engine-like cycles for highly controllable spin-1/2 states.

A heat machine can have two possible regimes, corresponding to the engine-type and refrigerator-type cycles, as shown on the left in Fig. 1. The right panels of Fig. 1 show their respective realizations using a two-

level system with modulated energy levels. Consider first the situation when the period of the drive $2\pi/\Omega$ is much larger than the decoherence time T_2 , which we denote as the *incoherent* regime. Figure 1(b) corresponds to the situation when the resonant driving increases the upper-level occupation during the large-energy-gap stage [A in Fig. 1(b)], followed by a relaxation to the ground state [C in Fig. 1(b)]. This is analogous to the heat-engine cycle in Fig. 1(a). For another choice of parameters, Figure 1(d) illustrates the situation when the resonant driving increases the upper-level occupation during the small-energy-gap stage “C”, with the relaxation during stage “A”; this is analogous to the refrigerator cycle in Fig. 1(c).

Note the similarity between our heat-engine-like cycles and the so-called Sisyphus lasing and cooling cycles, which also describe the periodic evolution of a modulated dissipative two-level system, studied in Refs. [26–30]. These processes take place when the period of the energy-level modulation is comparable to the relaxation time. Then the cycle has four stages: resonant excitation into the upper state, adiabatic evolution within this state, relaxation to the ground state, and again adiabatic evolution.

When decreasing the ratio of the driving period, $2\pi/\Omega$, to the decoherence time T_2 , we expect that the coherence will result in interference between the wave-function components [31–34]. This regime, when $T_2 \gtrsim 2\pi/\Omega$, can be denoted as a *coherent* regime. In this paper we study both the incoherent quantum “heat” cycles, like in Fig. 1, and coherent dynamics, resulting in interference fringes. We study a two-level system with modulated energy levels being driven by a periodic frequency-modulated signal, which makes the device highly controllable by several parameters (including the frequency and the amplitude of modulations). We present an experimental realization and a theoretical description of such a system, realized as an electron spin of an impurity placed in a silicon tun-

*E-mail address: k-ono@riken.jp

†E-mail address: sshevchenko@ilt.kharkov.ua

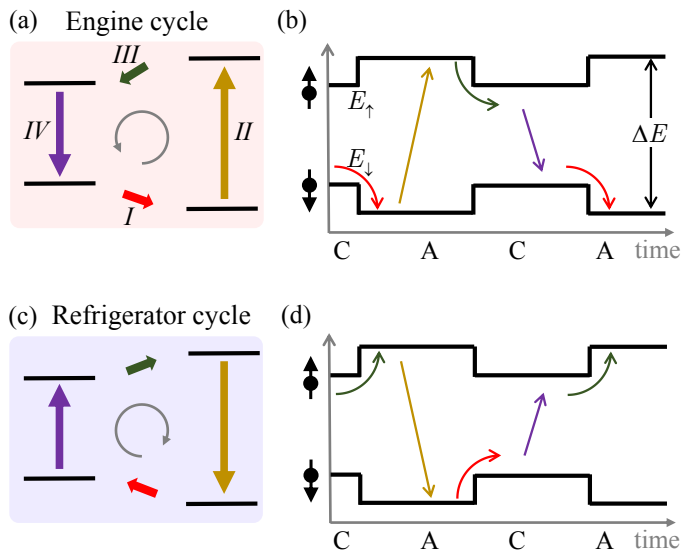


FIG. 1: Interpretation of the modulated dynamics in terms of a heat engine or a refrigerator. The heat-engine-like cycle, shown in (a), can be realized by modulating the energy levels, as shown in (b). The energy-level gap ΔE varies between larger, A, and smaller, C, values. The arrows show the incoherent dynamics with resonant excitation during the large-energy-gap stage A. Panels (c) and (d) present the incoherent dynamics with resonant excitation during the small-energy-gap stage, which is reminiscent of the refrigerator cycle.

nel field-effect transistor (TFET). Such system allows a versatile control via the microwave driving and the modulation of the Landé g -factor. Note that almost all works on quantum heat engines have been theoretical. Our device has the potential to realize these experimentally.

Device.—Our spin-qubit device is based on a short-channel TFET. Deep impurities are intensively ion-implanted to the channel of the TFET. At room temperature they act as quantum dots [35]. For a device with a channel length of ~ 80 nm, under a source voltage V_S and a gate voltage V_G , the source-to-drain conduction is dominated by tunneling through two impurities, i.e., one deep impurity and a shallow impurity located near the deep impurity. For more details, see the Supplemental Material (SM) [36].

This double-dot-like transport exhibits spin blockade phenomena [37–40], and enables the time-ensemble measure of an electron spin of one of the impurities. We focused on the small source-drain current under the spin blockade condition. Under appropriate dc and ac magnetic fields, the source-drain current increases due to the lifting of the spin blockade by the electron spin resonance (ESR) of one of the impurities [41]. Thus sweeping the frequency of the ac component of the magnetic field, for a fixed dc magnetic field, the source-drain current shows a peak at the ESR frequency, and the peak’s height is proportional to the excitation probability of the spin qubit.

We measure the spin-blockade source-drain current of

the device at 1.6 K with dc magnetic field $B \approx 0.28$ T and ac magnetic field with microwave (MW) frequency ~ 9 GHz. An observed linewidth of ~ 4 MHz, as well as a Rabi oscillation measurement [35], show a coherence time of $0.25 \mu\text{s}$. This timescale includes the effect of finite lifetime of the spin on the impurity. This finite lifetime is due to the finite mean-stay time of the electron on the impurity in the tunneling transport through the impurities. Thus the spin on the impurity is replaced at this timescale. Theoretically, this situation is described by introducing the phenomenological relaxation and decoherence times: $T_{1,2}$. For a two-level system, T_1 describes the relaxation from the excited state, while T_2 describes the lifetime of the coherence in the system.

Qubit energy modulation.—We found that the g -factor of one of the impurities can be tuned by the gate voltage V_G . This is due to the Stark effect [42]. In our device $\sim 1\%$ of the g -factor can be tuned by changing V_G within ± 20 mV. Note that the spin-blockade condition is still kept in our device if we change V_G by such amount. The fast modulation of V_G , and thus the energy of the spin qubit, are carried out by adding the radio frequency modulation to the gate electrode. Square waves with frequencies from 0.05 to 10 MHz are used. See Refs. [35, 42] for further details on the device, spin qubit measure, and V_G modulation; and see Refs. [9, 43, 44] for the study of other modulation pulses; in particular, the ones realizing the counter-diabatic driving.

MW frequency modulation.—We use the frequency modulation (FM) function of our MW generator, where the FM is proportional to the voltage signal fed to the external input. The two-channel arbitrary waveform generator was used for the V_G modulation, and the voltage was used for microwave frequency modulation. It is important to note that the bandwidth of the arbitrary waveform generator is ~ 100 MHz, so this modulation never excites higher-lying spin states, including the $1/2$ -spin of another impurity whose ESR frequency is 1 GHz higher than the focused spin. Thus, changes of both the qubit energy and MW frequency can be regarded as adiabatic. For the synchronized modulation of both the qubit energy and the MW frequency, we used two square-wave signals with tunable amplitudes and phase difference, and fed one signal to the gate electrode and another one to the input for the FM signal on the MW generator.

Theoretical description.— We describe this spin-qubit device as a driven two-level system, which is amplitude- and frequency- modulated, with the pseudo-spin Hamiltonian $H(t) = B_z(t)\sigma_z/2 + B_x(t)\sigma_x/2$. In other words, we consider a single $1/2$ -spin subject to a fast microwave driving and a slow rf modulation of both amplitude and frequency. Note that in our previous work [42] we only considered amplitude modulation.

The longitudinal part of the Hamiltonian $H(t)$ is defined by the Zeeman splitting, $B_z(t) = g(t)\mu_B B$. The time-dependent gate voltage changes the g -factor by a small value [45] and we have $B_z/\hbar = \omega_q + \delta\omega_q s(t)$, with $\delta\omega_q \ll \omega_q$, where $\omega_q = 2\pi f_q$ represents the ESR fre-

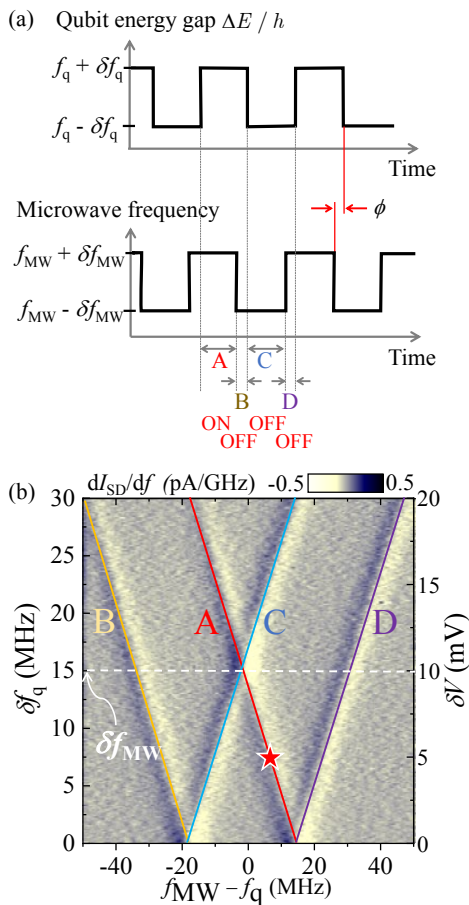


FIG. 2: Amplitude- and frequency-modulated two-level system. In the upper panel of (a) the qubit energy $\Delta E(t) = E_{\uparrow} - E_{\downarrow} = h[f_q + \delta f_q s(t)]$ is shown to be modulated in amplitude; in the lower panel, the modulated driving (microwave) frequency $f_{\text{FM}}(t) = f_{\text{MW}} + \delta f_{\text{MW}} s_{\phi}(t)$ is presented. The phase shift ϕ corresponds to four stages of evolution, denoted from A to D. We show the situation when the qubit is resonantly excited during the stage “A”, as in Fig. 1(b). Then the coupling between the drive and the qubit is “ON” during this stage and “OFF” during the other stages. The four possible resonant excitations are shown by the inclined lines in (b), where the colors correspond to the four stages in (a). Panel (b) presents the derivative of the source-drain current as a function of the frequency detuning and the amplitude of the energy-level modulation at $\delta f_{\text{MW}} = 15$ MHz.

quency, and $\delta\omega_q$ describes the *amplitude modulation*. In this work, we consider a square-wave modulation $s(t) = \text{sgn}[\cos \Omega t]$. The transverse part of the Hamiltonian is defined by the frequency-modulated MW voltage applied to the substrate, $B_x/\hbar = 2G \cos[\omega_{\text{FM}}(t)t]$, with a frequency $\omega_{\text{FM}}(t) = \omega_{\text{MW}} + \delta\omega_{\text{MW}} s_{\phi}(t)$, which is modulated by the phase-shifted signal $s_{\phi}(t) = \text{sgn}[\cos(\Omega t + \phi)]$. Here G stands for the amplitude, which is defined by the microwave power at the microwave-generator output and $\omega_{\text{MW}} = 2\pi f_{\text{MW}}$ is the microwave circular frequency. The modulation is assumed to be slow, i.e. $\Omega \ll \omega_{\text{MW}}$, and

with a small amplitude, $\delta\omega_{\text{MW}} \ll \omega_{\text{MW}}$, where $\delta\omega_{\text{MW}}$ describes the *frequency modulation*. (About amplitude and frequency modulation, see also in Refs. [46–51].) With the Hamiltonian $H(t)$ we solve the Bloch equations, as described in detail in the SM [36], see also Refs. [52, 53]. Analytical stationary solutions of the Bloch equations allow us to obtain the upper-level occupation probability P_+ , as shown in the lower part of Fig. 3, while the numerical solution gives the time-dependent occupation $P_+(t)$ [36].

The modulated qubit energy levels $E_{\uparrow,\downarrow} = \pm \frac{1}{2} \Delta E = \pm \frac{\hbar}{2} [\omega_q + \delta\omega_q s(t)]$ are plotted as a function of the dimensionless time $\tau = \Omega t/2\pi$ in the upper panel in Fig. 2(a). The lower panel of Fig. 2(a) presents the time dependence of the modulated microwave frequency $\omega_{\text{FM}}(t)$. This frequency is phase shifted with respect to the energy-level modulation.

The qubit experiences a resonant excitation when $\Delta E(t) = \hbar\omega_{\text{FM}}(t)$. This relation, written as $\omega_q + \delta\omega_q s(t) = \omega_{\text{MW}} + \delta\omega_{\text{MW}} s_{\phi}(t)$, allows four possibilities for the resonant excitation: $\Delta\omega \equiv \omega_q - \omega_{\text{MW}} = \Delta\omega^{(A,B,C,D)}$, where $\Delta\omega^{(A,B)} = -\delta\omega_q \pm \delta\omega_{\text{MW}}$ and $\Delta\omega^{(C,D)} = \delta\omega_q \mp \delta\omega_{\text{MW}}$. This means that, if one of the conditions is met, $\Delta\omega = \Delta\omega^{(i)}$, then during the i -th stage the resonant condition is fulfilled.

Note that the above conditions are valid for relatively small modulation frequencies, when the respective period is much larger than the decoherence time, $2\pi/\Omega \gg T_2$. In this case, the incoherent dynamics during one of the stages does not influence the dynamics of the later stages. And indeed, in the source-drain current the four resonance conditions were observed as the inclined lines along $\Delta\omega = \Delta\omega^{(A\dots D)}$, Fig. 2(b).

Specifically, we show schematically the resonant excitation in Fig. 2(a) and Fig. 1(b) for the situation when the resonant condition is for the stage “A”, where $\Delta\omega = \Delta\omega^{(A)}$. In Fig. 1(b) we start from the system in the ground state; then the qubit becomes partially excited; and later on we have full relaxation back to the ground state. This is shown for the incoherent regime. In the coherent regime, the relaxation time of the population is longer than the driving period (so that $T_2 \gtrsim 2\pi/\Omega$) and the interference between different stages takes place, which we will consider later in more detail.

Analogy to a heat engine.— First, it is possible to introduce an (effective) temperature T as the value defining the energy-level populations P_+ and $P_- = 1 - P_+$ with the relation $\frac{P_-}{P_+} = \exp\left(\frac{\Delta E}{k_B T}\right)$ [54, 55]. Then the driven and relaxed stages, with P_+ close to 1/2 and 0 respectively, determine the cold and hot reservoir temperatures [25]. The emulation of a quantum heat engine is then completed by associating the energy-level distance ΔE with the volume of a working gas in the corresponding macroscopic engine [25, 54]. With these, we are prepared to describe the driven evolution of our single-spin quantum machine.

We now consider, for simplicity, $\phi = 0$, while a non-

zero phase shift ϕ gives an additional degree of control. Then the stages D and B in Fig. 2(a) collapse and we have the alternation of the stages A and C only, as in Fig. 1. We start in Fig. 1(a,b) with $\Delta\omega = \Delta\omega^{(A)}$. Then the changes in the energy-level populations are shown by the four arrows, with the resonant excitation to the upper level shown by the dark yellow arrow and relaxation to the ground state shown by the violet arrow. Such evolution is equivalently drawn in Fig. 1(a), which behaves like a four-stroke quantum Otto engine [4]. During the stage I , the energy difference ΔE increases, corresponding to an expansion. The resonant drive during the stage II increases the upper-level population P_+ , as if in contact with a hot thermal reservoir. Then we have the compression during the stage III . Finally, the relaxation during the stage IV plays the role of contacting with a cold thermal reservoir, with decreasing P_+ .

An analogous evolution with the resonant excitation in the stage “ C ” is presented in Fig. 1(c,d). Such cycle, shown in Fig. 1(c), is reminiscent of a four-stroke refrigerator.

We emphasize that the situation shown in Fig. 1 is for the fast relaxation case, $2\pi/\Omega \gg T_{1,2}$. If the modulating frequency Ω is increased, then these two values become comparable, $2\pi/\Omega \sim T_{1,2}$. Then the interference between the different stages can be considered as a superposition of the “heat-engine” and “refrigerator” cycles. In the measured source-drain current, such superposition results in interference fringes, which we present later.

Note that the analogy with a “heat engine” is a partial one. Differences include the lack of high- and low-temperature reservoirs. In our system, the source and the drain are tools to probe the qubit, not heat reservoirs. Namely, the electrodes are reservoirs of electrons, and are not directly related to thermal reservoirs. A hot (thermodynamic) reservoir has more energy than a cold (thermodynamic) reservoir. An electronic analog of this would be this: a higher-voltage (electron) reservoir has more energy than a lower-voltage (electron) reservoir.

Slow-modulation regime.— The measured source-drain current I_{SD} is shown in Fig. 2(b) as a function of the driving microwave frequency f_{MW} and the amplitude of the energy-level modulation δf_q for a low-frequency ($\Omega/2\pi = 0.05$ MHz) square modulation, and the phase difference of two modulations $\phi = 90$ degrees. The four lines of the ESR peaks are seen in Fig. 2(b) at such value of ϕ . Next, we vary the phase difference ϕ between the two square-wave modulations, shown in Fig. 3(a). While fixing the two amplitudes of the square modulations to $\delta f_{MW} = \delta f_q$, the phase difference ϕ is changed from 0 to 360 degrees. The heights of the three ESR peaks are changed as in Fig. 3(a). At $\phi = 0$, the height of the center peak is maximum and two side peaks disappear. The condition with $\phi = 0$ and $f_{MW} - f_q = 0$ can be called *in-phase*, where the phase of the two modulations matches and the qubit is always in resonance with the microwaves. In contrast, at $\phi = 180$ deg., the center peak disappears and the heights of two side peaks have their

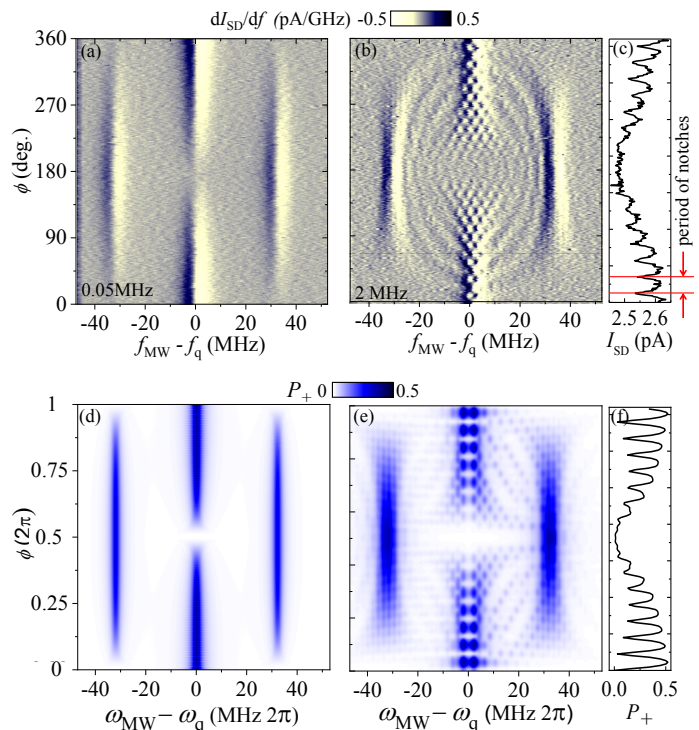


FIG. 3: Incoherent and coherent regimes at $\delta f_{MW} = \delta f_q$. Source-drain current I_{SD} as a function of the frequency detuning ($f_{MW} - f_q$) and the phase difference ϕ , in the incoherent (a) and coherent (b) regimes, for the modulation frequencies $\Omega/2\pi = 0.05$ and 2 MHz, respectively. (c) is the cross-section of (b) along the line $f_{MW} = f_q$. (d)-(f) show the respective upper-level occupation probability. Note the small “notches” in (b,c) and (e,f).

maximum. At this *out-of-phase* condition, $\phi = 180$ deg. and $f_{MW} - f_q = 0$, the qubit is always driven out of resonance. The height of the center ridge evolves linearly from its maximum (at the in-phase condition) to zero (at the out-of-phase condition), Fig. 3(a). The height simply reflects the duration of the “ON” stage, when the microwave is in resonance with the qubit, see Fig. 2(a).

Fast modulation: interference pattern.— Now we increase the modulation frequency up to around T_2^{-1} . Figure 3(b) shows an intensity plot similar to Fig. 3(a), but now the modulation frequency Ω is set to 2 MHz. In Figure 3(b) there are three vertical ridges, and their positions and heights are similar to the case of the slow modulation. However, there are many fringes in the interference pattern. A ripple-like pattern is seen between the center and side ridges. The edges of the ridges show fan-shaped broadenings, and, importantly, fine periodic interference patterns appear only around the central ridge. Similar to the slow modulation, the central ridge height is maximal at the in-phase condition and zero at the out-of-phase condition. However, due to this interference pattern, the ϕ dependence of the central ridge height shows a “beating” pattern with periodically appearing notches

[a cross-section shown in Fig. 3(c)].

We repeat similar measurements with various modulation frequencies, modulation amplitudes, and MW power [36]. For each setting, we repeat similar calibrations as in Fig. 3, and make sure that the condition $\delta f_{\text{MW}} = \delta f_{\text{q}}$ is met. We focus on the period of the notches observed on the central ridge, as indicated in Fig. 3(c), as a characteristic parameter of the interference. The results of calculations are presented in Fig. 3(d-f). The period of the notches is proportional to the modulation frequency Ω , i.e. $\Delta\phi/2\pi = \Omega/\delta\omega_{\text{MW}}$, inversely proportional to the modulation amplitude $\delta\omega_{\text{q}}$, i.e. $\Delta\phi/2\pi = \Omega/\delta\omega_{\text{q}}$, and independent of the microwave power G [36].

Conclusion.— We presented a detailed study of an energy- and frequency-modulated two-level system. The experimental realization of this was a spin-qubit device, based on a deep impurity in a short-channel silicon TFET. This was shown to work analogously to a heat engine or a refrigerator in the incoherent regime, at slow energy-gap modulation; and displaying interference fringes in the coherent regime, when the modulation period becomes larger than the decoherence time. Note that the coexistence of a classical heat pump and a refrigerator would functionally cancel each other; whereas the quantum superposition of an engine and a cooler exhibits

novel interferometric effects. Due to such interference, the quantum thermodynamic system can quickly switch its function between engine or refrigerator regimes, and respond fast to external signals, which is not possible with classical systems. Our impurity-based spin-qubit system has a set of parameters which reliably control its state. This makes it useful for possible applications, such as a future universal quantum heat engine.

Acknowledgments

We thank Ken Funo, Neill Lambert, and M. Fernando Gonzalez-Zalba for discussions. This work was supported by JST CREST JPMJCR1871, MEXT Q-LEAP JPMXS0118069228, JSPS KAKENHI 15H04000, 17H01276. F.N. is supported in part by: NTT Research, Army Research Office (ARO) (Grant No. W911NF-18-1-0358), Japan Science and Technology Agency (JST) (via Q-LEAP and the CREST Grant No. JPMJCR1676), Japan Society for the Promotion of Science (JSPS) (via the KAKENHI Grant No. JP20H00134, and the grant JSPS-RFBR Grant No. JPJSBP120194828), and the Grant No. FQXi-IAF19-06 from the Foundational Questions Institute Fund (FQXi), a donor advised fund of the Silicon Valley Community Foundation. Research of S.N.S. was sponsored by the Army Research Office and was accomplished under Grant Number W911NF-20-1-0261.

-
- [1] J. Gemmer, M. Michel, and G. Mahler, *Quantum Thermodynamics* (Springer, Berlin Heidelberg New York, 2004).
- [2] H. T. Quan, Y.-x. Liu, C. P. Sun, and F. Nori, “Quantum thermodynamic cycles and quantum heat engines,” *Phys. Rev. E* **76**, 031105 (2007).
- [3] R. Kosloff and A. Levy, “Quantum heat engines and refrigerators: Continuous devices,” *Ann. Rev. Phys. Chem.* **65**, 365–393 (2014).
- [4] J. Goold, M. Huber, A. Riera, L. del Rio, and P. Skrzypczyk, “The role of quantum information in thermodynamics—a topical review,” *J. Phys. A: Math. Theor.* **49**, 143001 (2016).
- [5] S. Vinjanampathy and J. Anders, “Quantum thermodynamics,” *Contemp. Phys.* **57**, 545–579 (2016).
- [6] S. Bhattacharjee and A. Dutta, “Quantum thermal machines and batteries,” arXiv:2008.07889 (2020).
- [7] R. Uzdin, A. Levy, and R. Kosloff, “Equivalence of quantum heat machines, and quantum-thermodynamic signatures,” *Phys. Rev. X* **5**, 031044 (2015).
- [8] J. Klatzow, J. N. Becker, P. M. Ledingham, C. Weinzetl, K. T. Kaczmarek, D. J. Saunders, J. Nunn, I. A. Walmesley, R. Uzdin, and E. Poem, “Experimental demonstration of quantum effects in the operation of microscopic heat engines,” *Phys. Rev. Lett.* **122**, 110601 (2019).
- [9] K. Funo, N. Lambert, B. Karimi, J. P. Pekola, Y. Masuyama, and F. Nori, “Speeding up a quantum refrigerator via counterdiabatic driving,” *Phys. Rev. B* **100**, 035407 (2019).
- [10] D. Gelbwaser-Klimovsky, R. Alicki, and G. Kurizki, “Minimal universal quantum heat machine,” *Phys. Rev. E* **87**, 012140 (2013).
- [11] P. A. Erdman, V. Cavina, R. Fazio, F. Taddei, and V. Giovannetti, “Maximum power and corresponding efficiency for two-level heat engines and refrigerators: optimality of fast cycles,” *New J. Phys.* **21**, 103049 (2019).
- [12] R. Dann, R. Kosloff, and P. Salomon, “Quantum finite-time thermodynamics: insight from a single qubit engine,” arXiv:2009.02801 (2020).
- [13] I. Buluta, S. Ashhab, and F. Nori, “Natural and artificial atoms for quantum computation,” *Rep. Prog. Phys.* **74**, 104401 (2011).
- [14] T. E. Humphrey, R. Newbury, R. P. Taylor, and H. Linke, “Reversible quantum brownian heat engines for electrons,” *Phys. Rev. Lett.* **89**, 116801 (2002).
- [15] H. T. Quan, Y. D. Wang, Y.-x. Liu, C. P. Sun, and F. Nori, “Maxwell’s demon assisted thermodynamic cycle in superconducting quantum circuits,” *Phys. Rev. Lett.* **97**, 180402 (2006).
- [16] O. Abah, J. Roßnagel, G. Jacob, S. Deffner, F. Schmidt-Kaler, K. Singer, and E. Lutz, “Single-ion heat engine at maximum power,” *Phys. Rev. Lett.* **109**, 203006 (2012).
- [17] M. Campisi, R. Blattmann, S. Kohler, D. Zueco, and P. Hänggi, “Employing circuit QED to measure nonequilibrium work fluctuations,” *New J. Phys.* **15**, 105028 (2013).
- [18] M. Campisi, J. Pekola, and R. Fazio, “Nonequilibrium fluctuations in quantum heat engines: theory, example, and possible solid state experiments,” *New J. Phys.* **17**, 035012 (2015).
- [19] G. Marchegiani, P. Virtanen, F. Giazotto, and M. Campisi, “Self-oscillating Josephson quantum heat engine,” *Phys. Rev. Applied* **6**, 054014 (2016).
- [20] B. Karimi and J. P. Pekola, “Otto refrigerator based on

- a superconducting qubit: Classical and quantum performance,” *Phys. Rev. B* **94**, 184503 (2016).
- [21] P. A. Erdman, F. Mazza, R. Bosisio, G. Benenti, R. Fazio, and F. Taddei, “Thermoelectric properties of an interacting quantum dot based heat engine,” *Phys. Rev. B* **95**, 245432 (2017).
- [22] M. Josefsson, A. Svilans, A. M. Burke, E. A. Hoffmann, S. Fahlvik, C. Thelander, M. Leijnse, and H. Linke, “A quantum-dot heat engine operating close to the thermodynamic efficiency limits,” *Nature Nanotech.* **13**, 920 (2018).
- [23] J. Roßnagel, S. T. Dawkins, K. N. Tolazzi, O. Abah, E. Lutz, F. Schmidt-Kaler, and K. Singer, “A single-atom heat engine,” *Science* **352**, 325–329 (2016).
- [24] G. Maslennikov, S. Ding, R. Hablützel, J. Gan, A. Roulet, S. Nimmrichter, J. Dai, V. Scarani, and D. Matsukevich, “Quantum absorption refrigerator with trapped ions,” *Nature Comm.* **10**, 202 (2019).
- [25] D. von Lindenfels, O. Gräß, C. T. Schmiegelow, V. Kaushal, J. Schulz, M. T. Mitchison, J. Goold, F. Schmidt-Kaler, and U. G. Poschinger, “Spin heat engine coupled to a harmonic-oscillator flywheel,” *Phys. Rev. Lett.* **123**, 080602 (2019).
- [26] M. Grajcar, S. H. W. Van der Ploeg, A. Izmalkov, E. Il’ichev, H.-G. Meyer, A. Fedorov, A. Shnirman, and G. Schön, “Sisyphus cooling and amplification by a superconducting qubit,” *Nature Phys.* **4**, 612–616 (2008).
- [27] F. Nori, “Superconducting qubits: Atomic physics with a circuit,” *Nature Phys.* **4**, 589–590 (2008).
- [28] J. C. Skinner, H. Prance, P. B. Stiffell, and R. J. Prance, “Sisyphus effects in a microwave-excited flux-qubit resonator system,” *Phys. Rev. Lett.* **105**, 257002 (2010).
- [29] S. N. Shevchenko, D. G. Rubanov, and F. Nori, “Delayed-response quantum back action in nanoelectromechanical systems,” *Phys. Rev. B* **91**, 165422 (2015).
- [30] M. J. Gullans, J. Stehlik, Y.-Y. Liu, C. Eichler, J. R. Petta, and J. M. Taylor, “Sisyphus thermalization of photons in a double quantum dot,” *Phys. Rev. Lett.* **117**, 056801 (2016).
- [31] S. N. Shevchenko, S. Ashhab, and F. Nori, “Landau-Zener-Stückelberg interferometry,” *Phys. Rep.* **492**, 1–30 (2010).
- [32] F. Forster, G. Petersen, S. Manus, P. Hänggi, D. Schuh, W. Wegscheider, S. Kohler, and S. Ludwig, “Characterization of qubit dephasing by Landau-Zener-Stückelberg-Majorana interferometry,” *Phys. Rev. Lett.* **112**, 116803 (2014).
- [33] K. C. Miao, A. Bourassa, C. P. Anderson, S. J. Whiteley, A. L. Crook, S. L. Bayliss, G. Wolfowicz, G. Thiering, P. Udvarhelyi, V. Ivady, H. Abe, T. Ohshima, A. Gali, and D. D. Awschalom, “Electrically driven optical interferometry with spins in silicon carbide,” *Sci. Adv.* **5** (2019).
- [34] R. M. Otxoa, A. Chatterjee, S. N. Shevchenko, S. Barraud, F. Nori, and M. F. Gonzalez-Zalba, “A quantum interference capacitor based on double-passage Landau-Zener-Stückelberg-Majorana interferometry,” *Phys. Rev. B* **100**, 205425 (2019).
- [35] K. Ono, T. Mori, and S. Moriyama, “High-temperature operation of a silicon qubit,” *Sci. Reports* **9**, 469 (2019).
- [36] See Supplemental Material at [URL will be inserted by publisher] .
- [37] K. Ono, D. Austing, Y. Tokura, and S. Tarucha, “Current rectification by Pauli exclusion in a weakly coupled double quantum dot system,” *Science* **297**, 1313–1317 (2002).
- [38] H. W. Liu, T. Fujisawa, Y. Ono, H. Inokawa, A. Fujiwara, K. Takashina, and Y. Hirayama, “Pauli-spin-blockade transport through a silicon double quantum dot,” *Phys. Rev. B* **77**, 073310 (2008).
- [39] G. Giavaras, N. Lambert, and F. Nori, “Electrical current and coupled electron-nuclear spin dynamics in double quantum dots,” *Phys. Rev. B* **87**, 115416 (2013).
- [40] K. Ono, G. Giavaras, T. Tanamoto, T. Ohguro, X. Hu, and F. Nori, “Hole spin resonance and spin-orbit coupling in a silicon metal-oxide-semiconductor field-effect transistor,” *Phys. Rev. Lett.* **119**, 156802 (2017).
- [41] F. H. L. Koppens, C. Buizert, K.-J. Tielrooij, I. T. Vink, K. C. Nowack, T. Meunier, L. P. Kouwenhoven, and L. M. K. Vandersypen, “Driven coherent oscillations of a single electron spin in a quantum dot,” *Nature* **442**, 766–771 (2006).
- [42] K. Ono, S. N. Shevchenko, T. Mori, S. Moriyama, and F. Nori, “Quantum interferometry with a g -factor-tunable spin qubit,” *Phys. Rev. Lett.* **122**, 207703 (2019).
- [43] J. Deng, Q.-h. Wang, Z. Liu, P. Hänggi, and J. Gong, “Boosting work characteristics and overall heat-engine performance via shortcuts to adiabaticity: Quantum and classical systems,” *Phys. Rev. E* **88**, 062122 (2013).
- [44] K. Funo, J.-N. Zhang, C. Chatou, K. Kim, M. Ueda, and A. del Campo, “Speeding-up a quantum refrigerator via counter-diabatic driving,” *Phys. Rev. Lett.* **118**, 100602 (2017).
- [45] G. Giavaras and Y. Tokura, “Probing the singlet-triplet splitting in double quantum dots: Implications of the ac field amplitude,” *Phys. Rev. B* **100**, 195421 (2019).
- [46] S. Savel’ev, F. Marchesoni, P. Hänggi, and F. Nori, “Transport via nonlinear signal mixing in ratchet devices,” *Phys. Rev. E* **70**, 066109 (2004).
- [47] S. Savel’ev, F. Marchesoni, P. Hänggi, and F. Nori, “Nonlinear signal mixing in a ratchet device,” *Europhys. Lett.* **67**, 179–185 (2004).
- [48] S. Ooi, S. Savel’ev, M. B. Gaifullin, T. Mochiku, K. Hirata, and F. Nori, “Nonlinear nanodevices using magnetic flux quanta,” *Phys. Rev. Lett.* **99**, 207003 (2007).
- [49] A. M. Satanin, M. V. Denisenko, A. I. Gelman, and F. Nori, “Amplitude and phase effects in Josephson qubits driven by a biharmonic electromagnetic field,” *Phys. Rev. B* **90**, 104516 (2014).
- [50] M. P. Silveri, J. A. Tuorila, E. V. Thuneberg, and G. S. Paraoanu, “Quantum systems under frequency modulation,” *Rep. Prog. Phys.* **80**, 056002 (2017).
- [51] S. Mondal, S. Bhattacharjee, and A. Dutta, “Exploring the role of asymmetric-pulse modulation in quantum thermal machines and quantum thermometry,” *Phys. Rev. E* **102**, 022140 (2020).
- [52] M. P. Silveri, K. S. Kumar, J. Tuorila, J. Li, A. Vepsäläinen, E. V. Thuneberg, and G. S. Paraoanu, “Stückelberg interference in a superconducting qubit under periodic latching modulation,” *New J. Phys.* **17**, 043058 (2015).
- [53] S. N. Shevchenko, *Mesoscopic Physics meets Quantum Engineering* (World Scientific, Singapore, 2019).
- [54] M. J. Henrich, F. Rempp, and G. Mahler, “Quantum thermodynamic Otto machines: A spin-system approach,” *Eur. Phys. J. Special Topics* **151**, 157–165 (2007).
- [55] G. Barontini and M. Paternostro, “Ultra-cold single-atom quantum heat engines,” *New J. Phys.* **21**, 063019 (2019).

Supplemental Material for:
Analog of a quantum heat engine using a single-spin qubit

K. Ono^{1,2}, S. N. Shevchenko^{3,4,5}, T. Mori⁶, S. Moriyama⁷, Franco Nori^{5,8}

¹*Advanced device laboratory, RIKEN,
Wako-shi, Saitama 351-0198, Japan*

²*CEMS, RIKEN, Wako-shi, Saitama 351-0198, Japan*

³*B. Verkin Institute for Low Temperature Physics and Engineering, Kharkov 61103, Ukraine*

⁴*V. N. Karazin Kharkov National University, Kharkov 61022, Ukraine*

⁵*Theoretical Quantum Physics Laboratory,
Cluster for Pioneering Research, RIKEN,
Wako-shi, Saitama 351-0198, Japan*

⁶*Device Technology Research Institute (D-Tech),
National Institute of Advanced Industrial Science and
Technology (AIST), Tsukuba, Ibaraki 305-8568, Japan*

⁷*Department of Electrical and Electronic Engineering,
Tokyo Denki University, Adachi-ku, Tokyo 120-8551, Japan and*

⁸*Department of Physics, The University of Michigan, Ann Arbor, MI 48109-1040, USA*

(Dated: September 15, 2020)

Abstract

In this Supplemental Material (SM) we present details of the device, experiment, and theory.

I. IMPURITY-BASED SPIN QUBIT

TFET-based device.— A tunnel field effect transistor (TFET) includes an n -type source electrode and a p -type drain electrode. Zener tunneling carries on-current, which flows between a channel driven to the p -type (or n -type) electrode by a gate voltage and the n electrode (p electrode), see Fig. S1. This TFET-based device is attracting attention as an ultra-low power consumption device because it enables steeper switching than conventional metal-oxide-semiconductor field effect transistors (MOSFETs). When a deep impurity is introduced into the channel of a TFET having a short channel length, which can be regarded as a gated PIN structure (with an undoped intrinsic semiconductor region between a p -type semiconductor and an n -type semiconductor region), a tunnel current flows through the impurity level even at the off-state of the TFET.

Our TFET-based devices are fabricated in much the same process as conventional MOSFETs. Using a 100 nm thick Si-on-insulator (SOI) wafer with 145 nm thick buried oxide (BOX), the source and drain are formed by shallow donor and acceptor ion implantation, respectively, and are activated by high temperature rapid thermal annealing. Next, Al and N are ion-implanted over the entire region consisting of source, channel, and drain, and annealing is performed for a long time at a relatively low temperature to form Al-N impurity pairs. A MOS gate is formed using TaN high-k / metal and poly-Si.

The electrical conductivity of these devices was probed at a temperature of 1.6 K. The source-drain current I_{SD} was measured while applying the gate voltage V_G and the source-drain voltage V_{SD} . A magnetic field B was applied in parallel to the source-drain current, and by applying a microwave current near the device, an ac magnetic field was generated and used for electron spin resonance (ESR). For the synchronized modulation of both the gate voltage and the microwave frequency, we used a two-channel square-waveform generator. The two square-wave signals have the same frequency and tunable amplitudes and phase difference. One of the square-wave signals is fed to the gate electrode of the device via a DC block capacitor so that the gate voltage is modulated by the square wave with an averaged DC voltage of V_G . The other square-wave signal is fed to an auxiliary input as an analog signal for the frequency modulation (FM) of the MW signal.

Without modulation.— The source-drain voltage V_{SD} and the gate voltage V_G of the device are set to satisfy the spin-blockade condition, where the source-drain current shows

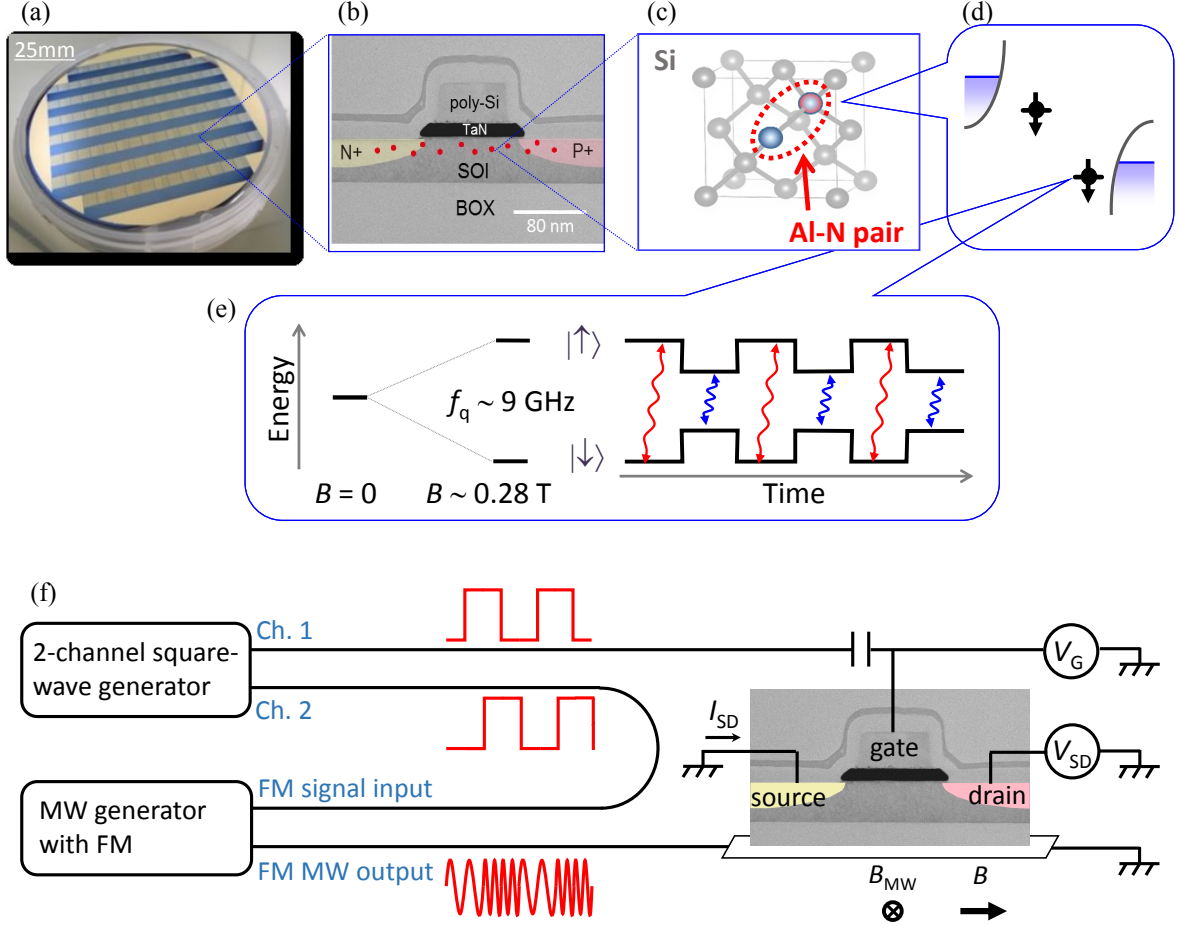


FIG. S1: Overview of device and its operation. The device is fabricated by standard CMOS processing technology with ion-implantations of Al and N, introducing Al-N impurity pairs as deep impurities. (a) Photo of a 4-inch wafer after the ion-implantation processing. (b) Cross-section image by a transmission electron microscope of the TFET-based device. (c) Schematic of an Al-N impurity pair in the unit cell of Si. (d) Schematic diagram of the potential energy landscape for PIN structure in the channel of the TFET with two impurity levels. Electron tunneling via a deep impurity and a shallow impurity exhibits both double-dot-like transport and spin blockade. (e) Schematic of the time evolution of one of the spin qubits. The qubit energy (Zeeman splitting) is modulated with a square-wave form $f_q \pm \delta f_q$. The applied microwave frequency is also modulated with a square-wave form $f_{MW} \pm \delta f_{MW}$. (f) Schematic of the measurement set up. A two-channel square-waveform generator and a MW generator with an FM signal are connected for the double modulation. Schematic wave forms are illustrated as red lines; a square wave from channel 1 (Ch. 1), a square wave from Ch. 2 that has a defined phase difference against the channel 1 signal, and the FM MW signal where its frequency is modulated by the channel 2 signal.

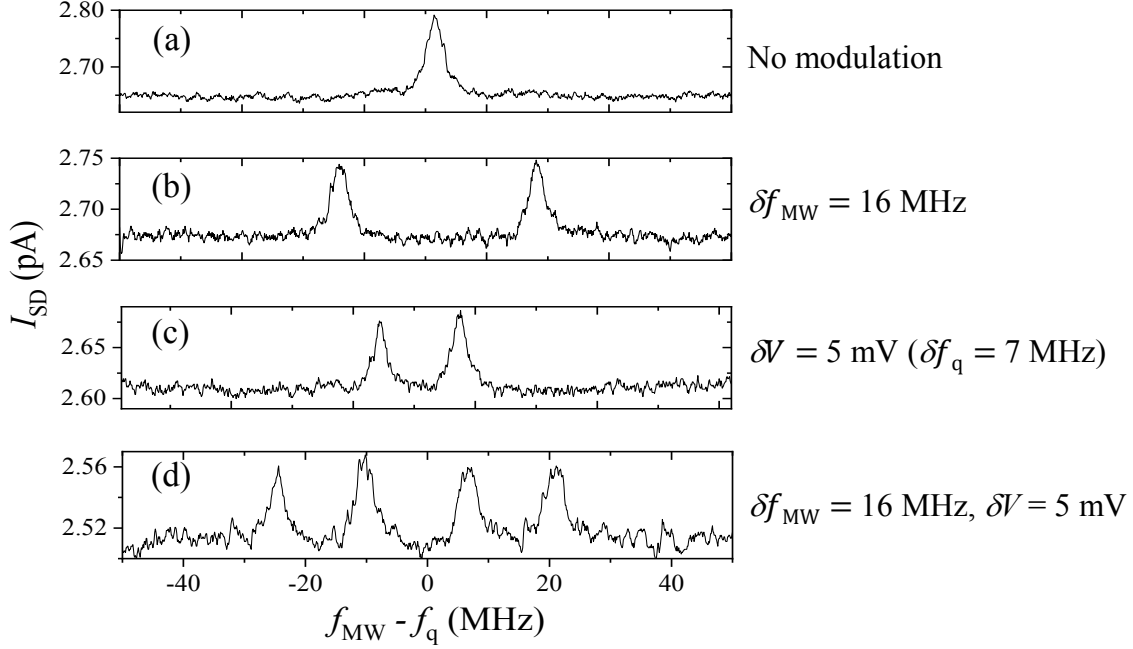


FIG. S2: Electron spin resonance (ESR) signal with and without modulation. (a) without any modulation, one ESR peak (at $f_{\text{MW}} = f_{\text{q}} = 9$ GHz) is observed in the source-drain current I_{SD} of the device in the spin-blockade regime. Two ESR peaks for the modulation of the microwave frequency (b) or for the modulation of the qubit energy (c). Panel (d) presents four ESR peaks when the two modulations are applied simultaneously.

an ESR response. Figure S2(a) shows the ESR signal without any modulation, with a single ESR peak observed where the microwave (MW) frequency f_{MW} matches the qubit frequency $f_{\text{q}} \sim 9$ GHz. The linewidth, or inverse coherence time $(T_2^*)^{-1} = 4$ MHz, is limited by the lifetime of the spin-blockade state, see Ref. [35] of the main text.

Slow amplitude modulation.— We first simultaneously apply the qubit energy modulation, with amplitude $2\delta f_{\text{q}}$, and a microwave frequency modulation (FM), with amplitude $2\delta f_{\text{MW}}$. Both of these modulations have a square-wave form.

In order to realize the condition where the high/low frequency microwave excites the large/small energy gap of the qubit, we tuned the parameters in the following manner. The waveform used for the FM is a square wave with frequency 0.05 MHz, which was set to be much smaller than the inverse coherence time $(T_2^*)^{-1}$. The amplitude of the square wave was set so that the microwave frequency is $f_{\text{MW}} \pm \delta f_{\text{MW}}$. Thus, if we sweep f_{MW} , the two ESR peaks appear at $f_{\text{MW}} - f_{\text{q}} = \pm \delta f_{\text{MW}}$ [Fig. S2(b)].

Then we also turn-on the qubit energy modulation by adding a square-wave modulation on V_G . By increasing the modulation amplitude δV_G from zero, each of the two ESR peaks is further split into two, and thus in total four peaks appear. Those four peaks correspond to four combinations where the qubit with energy $f_q \pm \delta f_q$ is excited by microwaves with frequency $f_{MW} \pm \delta f_{MW}$ [Fig. S2(d)]. Figure 2(b) of the main text shows the evolution of the ESR peaks increasing δV_G . The crossing of the lines of the ESR peaks appear at $\delta V_G = 11$ mV, where we see three peaks instead of four. The three peaks correspond to these three situations:

- (1) the qubit with frequency $(f_q - \delta f_q)$ is excited by microwaves with frequency $(f_{MW} + \delta f_{MW})$;
- (2) the qubit with $(f_q - \delta f_q)$ is excited by the microwave with $(f_{MW} - \delta f_{MW})$ and, at the same time, the qubit with $(f_q + \delta f_q)$ is excited by the microwave with $(f_{MW} + \delta f_{MW})$; and
- (3) the qubit with $(f_q + \delta f_q)$ is excited by the microwave with $(f_{MW} - \delta f_{MW})$. Thus, at the center peak (peak at the crossing) δf_{MW} is matched to δf_q . Now δV_G can be converted to δf_{MW} , as shown in the left axis of Fig. 2(b) of the main text.

II. THEORY OF AMPLITUDE- AND FREQUENCY-MODULATED SINGLE SPIN

A. Hamiltonian and master equation

We describe our device as a modulated and driven quantum two-level system with the pseudo-spin Hamiltonian

$$H(t) = B_z(t)\sigma_z/2 + B_x(t)\sigma_x/2. \quad (\text{S1})$$

To be more precise, we consider a single 1/2-spin with a fast microwave driving and a slow rf modulation of both amplitude and frequency. The longitudinal part is defined by the Zeeman splitting, $B_z(t) = g(t)\mu_B B$. The time-dependent gate voltage changes the g -factor by a small value and we have

$$B_z/\hbar = \omega_q + \delta\omega_q \cdot s(t), \quad \delta\omega_q \ll \omega_q, \quad (\text{S2})$$

Parameter	Description	Value or Range
ω_q	$= 2\pi f_q$, ESR frequency; this is defined by the magnetic field, $\omega_q \propto B$	$f_q = 9.0$ GHz at $B = 0.28$ T
$\delta\omega_q$	$= 2\pi\delta f_q$, amplitude of energy-level modulation; defined by the gate voltage modulation, $\delta\omega_q \propto \delta V$	$\delta f_q = 16$ MHz at $\delta V = 12$ mV
Ω	square-modulation frequency	$\Omega \in [0.05, 50]$ MHz $\cdot 2\pi$
ω_{MW}	$= 2\pi f_{\text{MW}}$, driving MW frequency	$\omega_{\text{MW}} = \omega_q - \Delta\omega$, $ \Delta\omega \leq 50$ MHz $\cdot 2\pi$
$\delta\omega_{\text{MW}}$	amplitude of frequency modulation	$\delta\omega_{\text{MW}} = 32$ MHz $\cdot 2\pi$
G	driving amplitude; this is defined by the microwave power at the MW-generator output, $G \propto \sqrt{P_{\text{MW}}}$	$G = 1$ MHz $\cdot 2\pi$ at $P_{\text{MW}} = 7$ dBm
ϕ	phase shift	$\phi \in [0, 360]$ degrees

TABLE I: Description of the parameters controlling our driven and modulated single-spin qubit

where $\omega_q = 2\pi f_q$ represents the ESR frequency, $\delta\omega_q$ describes the *amplitude modulation*. In this work, we consider a square-wave modulation with the signal

$$s(t) = \text{sgn}[\cos \Omega t]. \quad (\text{S3})$$

The transverse part of the Hamiltonian is defined by the frequency-modulated MW voltage applied to the substrate,

$$\begin{aligned} B_x/\hbar &= 2G \cos[\omega_{\text{FM}}(t)t], \\ \omega_{\text{FM}}(t) &= \omega_{\text{MW}} + \delta\omega_{\text{MW}} \cdot s_\phi(t), \\ s_\phi(t) &= \text{sgn}[\cos(\Omega t + \phi)], \end{aligned} \quad (\text{S4})$$

with amplitude G and microwave circular frequency $\omega_{\text{MW}} = 2\pi f_{\text{MW}}$. The modulation is assumed to be slow, i.e. $\Omega \ll \omega_{\text{MW}}$, and with a small amplitude, $\delta\omega_{\text{MW}} \ll \omega_{\text{MW}}$, where $\delta\omega_{\text{MW}}$ describes the *frequency modulation*. The theoretical and experimental parameters are collected in Table I.

After the unitary transformation $U = \exp(-i\omega_{\text{MW}}\sigma_z t/2)$ and the rotating-wave approxi-

mation, as in Refs. [35, 43, 45] of the main text, we obtain

$$H_1 = \frac{\hbar}{2} \left[\Delta\omega + \tilde{f}(t) \right] \sigma_z + \frac{\hbar G}{2} \sigma_x, \quad (\text{S5})$$

$$\tilde{f}(t) = \delta\omega_q \cdot s(t) - \delta\omega_{\text{MW}} \cdot s_\phi(t), \quad (\text{S6})$$

where $\Delta\omega = \omega_q - \omega_{\text{MW}} = 2\pi (f_q - f_{\text{MW}})$.

Then, the upper-level occupation probability P_+ is readily obtained from the stationary solution of the Bloch equations:

$$P_+ \left(\Delta\omega, \frac{\delta\omega_q}{\Omega} \right) = \frac{1}{2} \sum_{k=-\infty}^{\infty} \frac{G_k^2(\delta\omega_q/\Omega)}{G_k^2(\delta\omega_q/\Omega) + \frac{T_2}{T_1} (\Delta\omega - k\Omega)^2 + \frac{1}{T_1 T_2}}, \quad (\text{S7})$$

where $G_k(x) = G |\Delta_k(x)|$, which can be interpreted as the dressed qubit gap, modulated by the function $\Delta_k(x)$

$$\Delta_k = \int_0^1 d\tau \exp \left[-i2\pi k\tau + i \int_0^\tau d\tau' \tilde{f}(\tau') \right]. \quad (\text{S8})$$

The relaxation and decoherence times are denoted as T_1 and T_2 , respectively.

It is straightforward to calculate Δ_k using Eq. (S8) with the integrand $\tilde{f}(\tau)$ defined by Eq. (S6). The resulting expression for Δ_k consists of four terms, which have the denominators $-k \pm x \pm w$, respectively, with $x = \delta\omega_q/\Omega$ and $w = \delta\omega_{\text{MW}}/\Omega$. This defines the characteristic k 's for each term. And, respectively, the absolute values of Δ_k for these four terms are the following

$$|\Delta_k| = \left| \frac{\sin \left[\frac{\pi - \phi}{2} (k \mp (x - w)) \right]}{\pi (k \mp (x - w))} \right|, \quad \left| \frac{\sin \left[\frac{\phi}{2} (k \mp (x + w)) \right]}{\pi (k \mp (x + w))} \right|. \quad (\text{S9})$$

Consider now the limiting case $\Omega \rightarrow 0$, which describes the incoherent-regime resonances at $\Omega < 2T_2^{-1}$, as detailed in Ref. [35] of the main text. We then expect resonances along the lines

$$\Delta\omega = k\Omega = \pm\delta\omega_q \pm \delta\omega_{\text{MW}}. \quad (\text{S10})$$

An analysis of the four relations from Eq. (S9) in the limit $\Omega \rightarrow 0$ gives for $\phi \in [0, \pi]$

$$|\Delta_k| \simeq \frac{\phi}{2\pi} \quad \text{for } k \simeq \pm (\delta\omega_q + \delta\omega_{\text{MW}}), \quad (\text{S11})$$

$$|\Delta_k| \simeq \frac{\pi - \phi}{2\pi} \quad \text{for } k \simeq \pm (\delta\omega_q - \delta\omega_{\text{MW}}). \quad (\text{S12})$$

The above equations are useful for describing the experimental results, as detailed in the next Section.

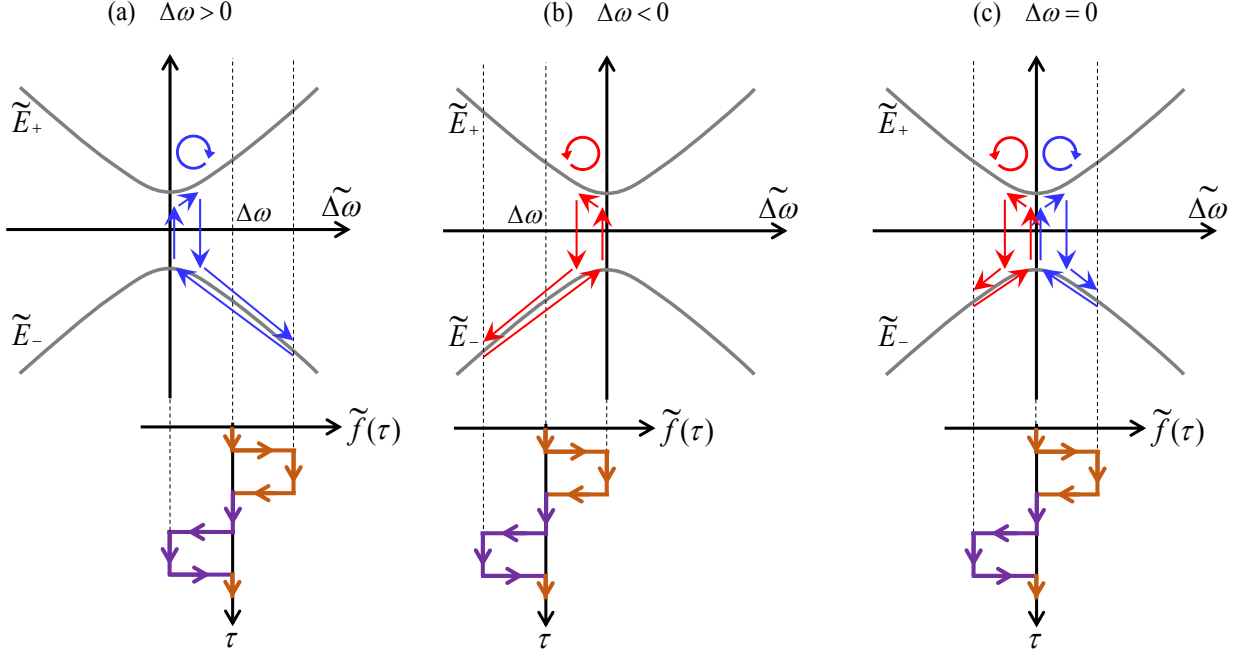


FIG. S3: Schematic of the refrigerator-like and engine-like cycles. The dressed energy levels \tilde{E}_{\pm} are plotted as a function of the modulation-defined frequency offset $\widetilde{\Delta\omega}$. The modulation $\tilde{f}(t)$ allows the system to oscillate between two limiting values, with a possible excitation at the avoided-level crossing and the subsequent relaxation. This is illustrated here for the incoherent regime, $\Omega/2\pi < 2T_2^{-1}$.

B. Dressed states and heat-engine-like cycles

Equation (S5) describes the qubit dressed by the microwave signal. The respective eigenstates are

$$\tilde{E}_{\pm} = \pm \frac{\hbar}{2} \sqrt{G^2 + \widetilde{\Delta\omega}^2}, \quad (\text{S13})$$

where $\widetilde{\Delta\omega} = \Delta\omega + \tilde{f}(t)$. In this way, the time dependence in $\tilde{f}(t)$ results in varying the distance between the dressed-state energy levels $\tilde{E}_+ - \tilde{E}_-$. The energy levels are plotted in Fig. S3. Then, we consider the dynamics forced by the modulation $\tilde{f}(t)$, around $\widetilde{\Delta\omega} = \Delta\omega$.

In figure S3, we consider the symmetric case with $\delta\omega_q = \delta\omega_{\text{MW}}$, which corresponds to the horizontal dashed line in Fig. 2(b) of the main text. Then the modulation $\tilde{f}(t)$ takes three values, 0 and $\pm 2\delta\omega_q$. We colour the curve for $\tilde{f}(t)$ in brown when this corresponds to the large-energy-gap half-period and in purple when this corresponds to the small-energy-gap half-period.

Then we consider three situations in Fig. S3(a-c), for $\Delta\omega = 2\delta\omega_q$, $-2\delta\omega_q$, and 0, respectively. In the situations (a) and (b), the qubit is excited during the small-energy-gap and large-energy-gap stages, respectively. For the incoherent regime, when $\Omega/2\pi < 2T_2^{-1}$, the system relaxes to the ground-state, and its evolution is shown by the blue and red trajectories. In terms of Fig. 1 of the main text, these correspond to the refrigerator-like and engine-like cycles. We mimic this by the blue and red round arrows in Fig. S3(a,b).

In the symmetric situation in Fig. S3(c), there are two cycles, both clockwise and counter-clockwise, during one modulation period. We emphasize that there is no crosstalk between the two cycles, since the relaxation is fast in the incoherent regime. In contrast, when increasing the modulation frequency so that $\Omega/2\pi \gtrsim 2T_2^{-1}$, i.e. going to the coherent regime, such cycles start to overlap. Essentially, *such superposition of the two cycles results in the constructive or destructive interference* with increased or suppressed upper-level occupation probability. We consider these interference fringes in detail both in the main text and below.

III. RESULTS

A. Experiments

Measurements as in Fig. 2(b) in the main text, for various ϕ , are shown in Fig. S4(a-e). In Fig. S4(f-j) we demonstrate the results of calculations related to the experimental ones in Fig. S4(a-e), respectively. Details of the calculations are described in the next subsection.

The dependence of the source-drain current I_{SD} on the square-wave modulation frequency Ω and the microwave frequency f_{MW} for $\delta f_{MW} = 0$ and $\delta V = 0$ are shown in Fig. S5(a) and Fig. S5(b), respectively.

Figure S6 shows measurements as in Fig. 3(b) in the main text but with different parameters, as written in each figure. We note that due to the delay of the two modulation signals, the phase difference depends on the modulation frequency within the MHz regime. Thus we redefine the $\phi = 0$ position so that the intensity plot image becomes symmetric.

These experimental data are all reproduced by our calculations. Figure S7 shows such calculated results, where the modulation-frequency dependence corresponds to Fig. S6(a-e); see details in the next subsection.

We extract the period of the notches from the data in Fig. S6 and summarize them in

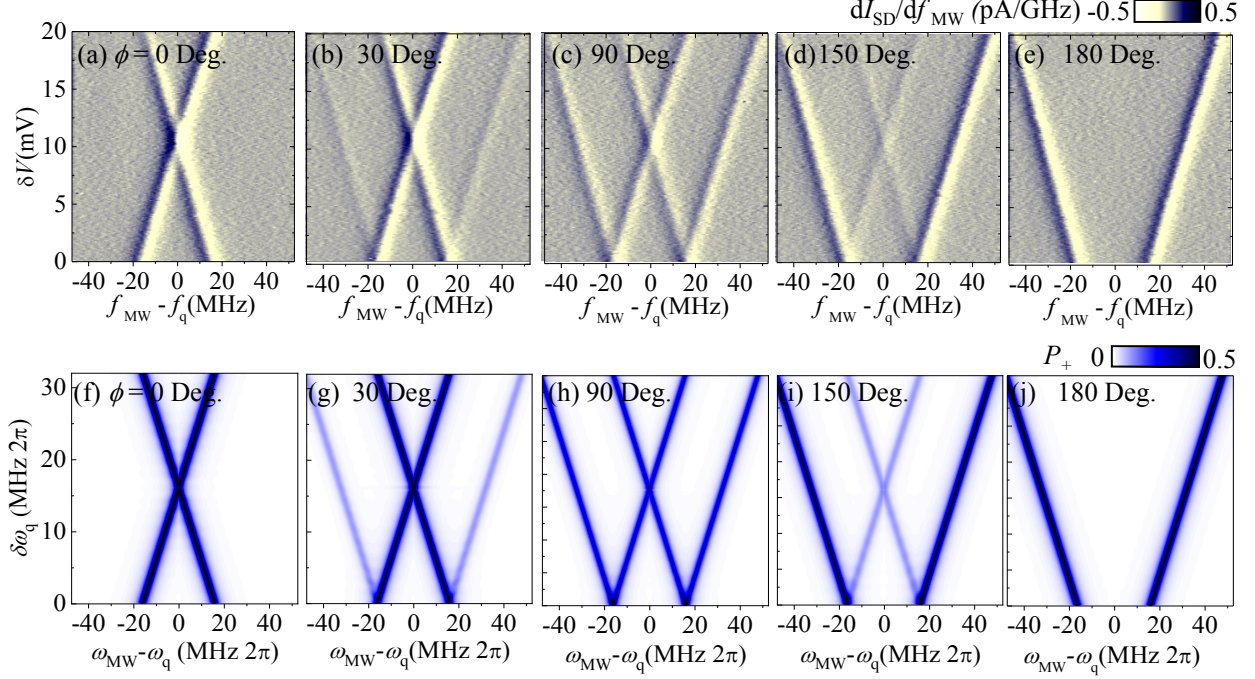


FIG. S4: The experimental source-drain current I_{SD} , top row, and the theoretical upper-level occupation probability P_+ , bottom row, as a function of the energy-level modulation amplitude $\delta\omega_q = \delta\omega_q(\delta V)$ and the microwave frequency $\omega_{MW} = 2\pi f_{MW}$. The data are similar to the ones in Fig. 2(b) of the main text, for various phase shifts ϕ ; the parameters are the same as in Fig. 2 of the main text, except of ϕ . The panels (a-e) and (f-j) show the experiment and calculations, respectively. For $\phi = 0$ the in-phase condition is met at $\delta V = 12$ mV, where $\delta f_q = \delta f_{MW}$, while the out-of-phase condition is met at $\delta V = 12$ mV and $\phi = 180$ deg.

Fig. S8, showing excellent agreement between the experiments and calculations.

Figure S9(b) shows one example of the measurements as in Fig. S4(a) ($\phi = 0$) for the fast modulation frequency $\Omega/2\pi = 2$ MHz. The X-shaped pattern in S9(b), similar to the one in Fig. S4(a), was obtained; but there are weak ripples around the pattern. Note that if ϕ is set at a notch [$\phi = 11$ deg., Fig. S9(c)], the X-shaped pattern shows a weak avoided crossing in the middle of the green dashed horizontal line in Fig. S9(c).

B. Theory

Using formulas (S7) and (S9) we can *quantitatively* describe the experimental results.

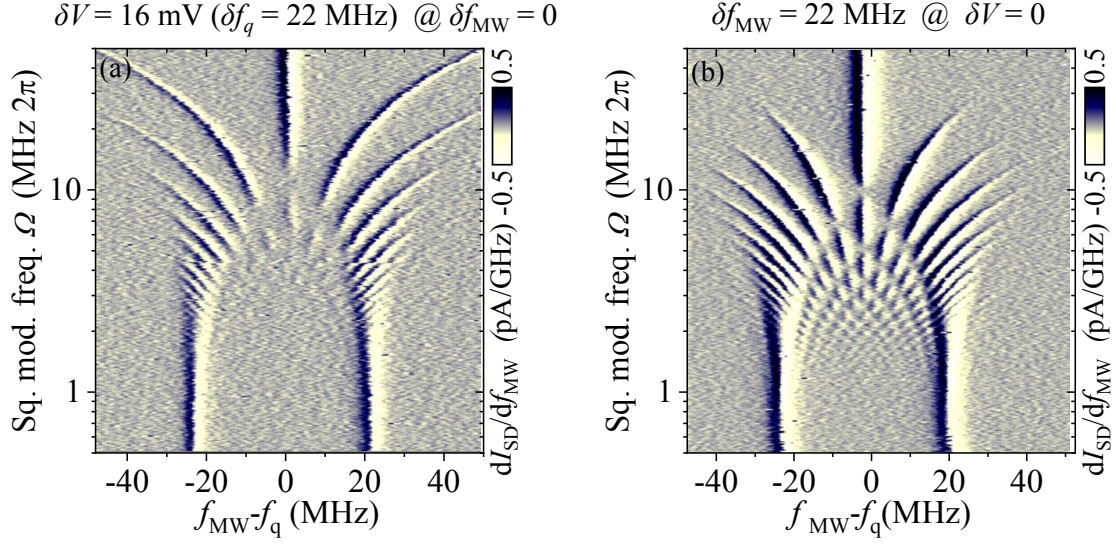


FIG. S5: Dependence of the source-drain current I_{SD} on the square-wave modulation frequency Ω and the microwave frequency f_{MW} for $\delta f_{MW} = 0$ (a) and $\delta V = 0$ (b). The amplitude of the modulation δV_G is fixed to 8 mV, which corresponds to $\delta f_q = 22$ MHz. The interference pattern is the same as discussed in Ref. [35] of the main text and agrees with the calculations. This ensures that square-wave signals up to 50 MHz can be applied to the gate without significant deformation of the waveform. In (b) the FM frequency of the microwave changes from 0.5 to 50 MHz. The amplitude δf_{MW} of the FM is fixed to 22 MHz. The interference pattern shows a cut-off of the sideband peaks for modulation frequencies larger than 10 MHz. Thus, we limit the FM modulation up to 5 MHz in the following measurements.

1. Incoherent regime

Consider, first, the incoherent regime, with $\Omega < 2T_2^{-1}$. This is described by the four possible resonance lines in Fig. 2 of the main text and Fig. S4, where the lower row was plotted making use of Eqs. (S7) and (S9). We note that the height and the width of the lines are defined by the phase shift ϕ .

In order to better understand the origin of the four lines in the W-shaped pattern in Fig. S4, consider now Eqs. (S11, S12). Then, at $\phi = 0$, the width of the lines, described by Eq. (S11), tends to zero, and we have two lines only at

$$\Delta\omega = \pm(\delta\omega_q - \delta\omega_{MW}), \quad (\text{S14})$$

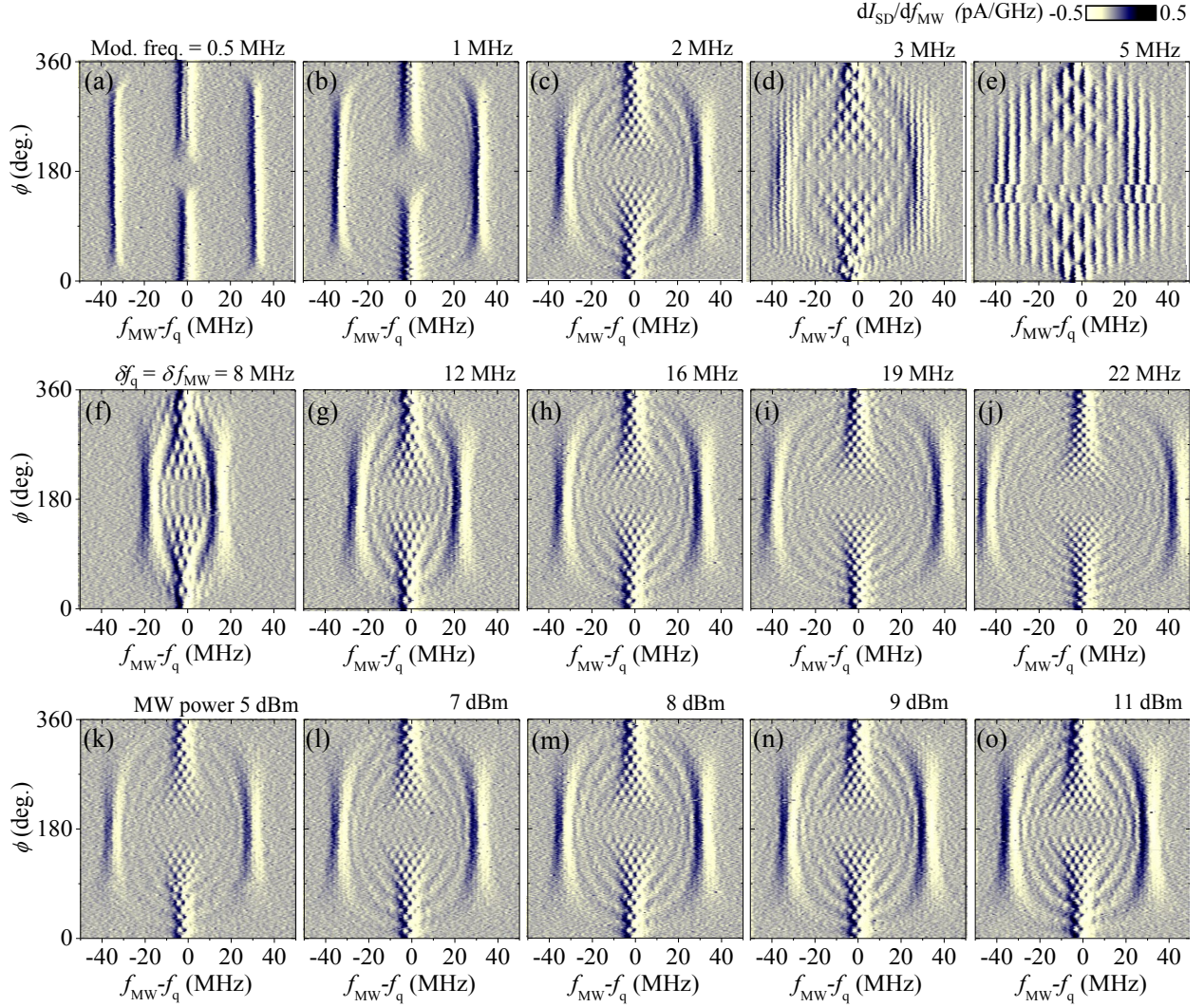


FIG. S6: Summary of the phase ϕ dependence, as in Fig. 3 of the main text, for various modulation frequencies Ω (a-e), various modulation amplitudes δf_{MW} (f-j), and various microwave powers P_{MW} (k-o). Parameters are the same as in Fig. 3, except the ones shown in this figure. For (f-j) similar measurements as in Fig. 2 were performed when $\delta f_{\text{q}} = \delta f_{\text{MW}}$.

which corresponds to the X-shaped lines in Fig. S4(f). They intersect at $\delta\omega_{\text{q}} = \delta\omega_{\text{MW}}$, which, importantly, can be useful for calibration of the power. Next, at $\phi = \pi$, the width of the lines, described by Eq. (S12), tends to zero, and we have two other lines, along

$$\Delta\omega = \pm(\delta\omega_{\text{q}} + \delta\omega_{\text{MW}}), \quad (\text{S15})$$

which corresponds to the V-shaped lines in Fig. S4(j). For other values of ϕ , we have all the four lines. Their widths become equal for $\phi = \pi/2$, Fig. S4(h).

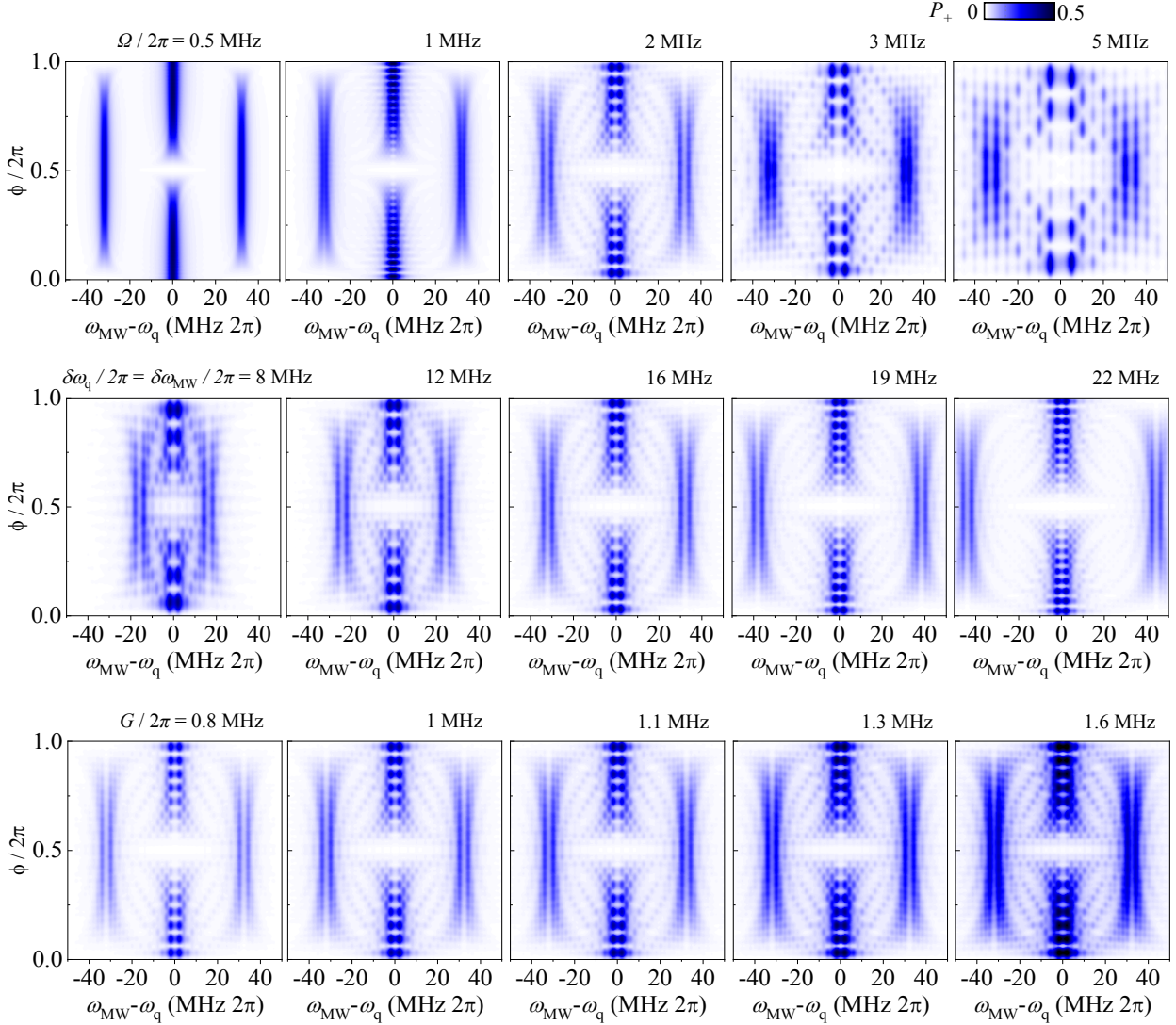


FIG. S7: Upper-level occupation probability P_+ as a function of the frequency detuning ($\omega_{\text{MW}} - \omega_{\text{q}}$) and the phase difference ϕ , for several values of the modulation frequency Ω (upper row), amplitude of energy-level modulation $\delta\omega_{\text{q}}$ (middle row), and driving amplitude G (lower row).

2. Coherent regime

To describe the coherent regime, with $\Omega \gtrsim 2T_2^{-1}$, as in Fig. S6, we again use Eqs. (S7) and (S9) to plot the upper-level occupation probability P_+ in the general case, for the respective parameters. Figure S7 presents the appearance of the interference fringes, where the upper-level occupation probability rapidly changes between 0 and 1/2. This figure correctly reproduces the experimental data in Fig. S6. Note that the upper panels of Fig. S6

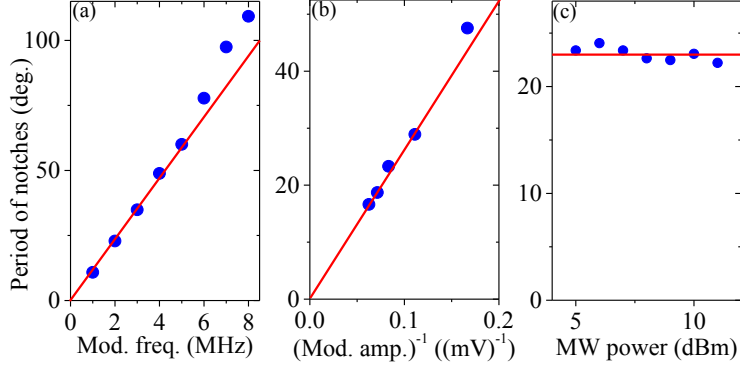


FIG. S8: Period of the notches (see Fig. 3 of the main text) as a function of the modulation frequency Ω , inverse modulation amplitude δV^{-1} , and the microwave power P_{MW} .

and Fig. S7 demonstrate how the interference fringes appear when increasing the modulation amplitude, starting from $\Omega = 0.5 \text{ MHz} \cdot 2\pi < 2T_2^{-1}$.

We call “notches” the suppression of the resonance lines down to $P_+ = 0$, see Fig. 3 of the main text. From Eq. (S9) it follows that the distance between the notches is defined by

$$\Delta\phi/2\pi = \Omega/\delta\omega_{\text{MW}} \propto \Omega \quad \text{and} \quad \Delta\phi/2\pi = \Omega/\delta\omega_{\text{q}} \propto \delta\omega_{\text{q}}^{-1}, \quad (\text{S16})$$

if changing Ω and $\delta\omega_{\text{q}}$, respectively. Importantly, the distance between the notches is proportional to the modulation frequency Ω , inversely proportional to the modulation amplitude $\delta\omega_{\text{q}}$, and is independent of the driving amplitude G , where the latter is defined by the MW power P_{MW} . These relations are demonstrated in Fig. S8(a, b, and c), respectively.

3. Dynamics

So far, we considered the stationary solution in order to describe the experimentally observed data. The obvious success in this allows us to claim that we have both the correct physical explanation of what happens and also the correct parameters. Then, with this, we can go further and solve numerically the Bloch equations to demonstrate the dynamics of the upper-level occupation probability.

The time evolution of the upper-level occupation probability $P_+(t)$ for the coherent case, with $\Omega/2\pi = 2 \text{ MHz}$, is shown in Fig. S10. For this we solved the time-dependent Bloch equations numerically, with different initial conditions. In a few cycles, the transient dynam-

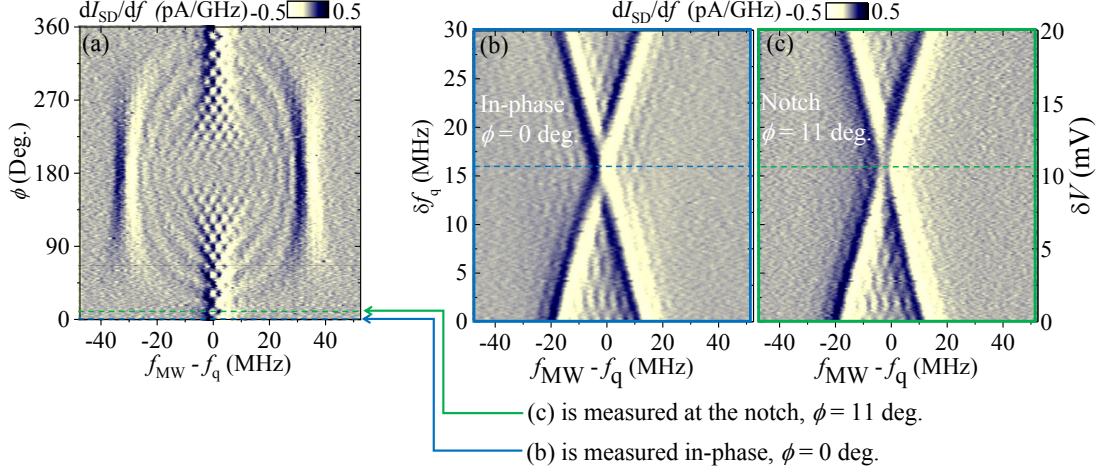


FIG. S9: Interference fringes in the dependence of the source-drain current I_{SD} for the X-shaped pattern. This is shown in (b) and (c) as a function of the frequency detuning ($f_{MW} - f_q$) and the amplitude δf_q of the energy-level modulation, for two values of the phase difference ϕ , which correspond to the lines shown in (a).

ics evolves into the stationary solution. Note that Fig. 3 of the main text and the graphs above show the time-averaged stationary solution, which corresponds to the upper-level occupation probability P_+ at times $t \gg T_{1,2}$. However, in principle, after preparing either the ground or excited state, we can start up our device following one of the trajectories in the main panel of Fig. S10 and quantify it by the extended efficiency e in the inset. The extended efficiency is introduced there so that $e = 1$ corresponds to a perfect engine, as in Fig. 1(a) of the main text, while $e = -1$ corresponds to a perfect refrigerator, as in Fig. 1(c). Coexistence and interference of these two cycles gives $e \in (-1, 1)$. A decoherence or complete mixing of these cycles leads to $e = 0$ and the system does not work as a heat engine anymore.

In order to see the dynamics in the experiment, after initializing the qubit, we would need a pulse-modulation of the drive frequency + qubit energy. The pulse length is expected to be about 0.1–1 μs from the previous Rabi oscillation experiment (Ref. [28]). However, such experiments have not been possible because the current experimental setup does not have enough equipment to perform this pulsing. Thus, the experiments on the dynamics are outside of the scope of this paper. In the future, we would like to conduct the pulse experiments related to our calculated predictions, shown in Fig. S10.

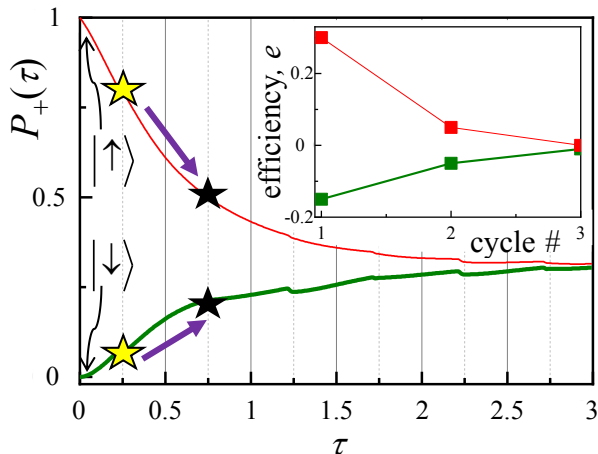


FIG. S10: Dynamics and the extended efficiency e . Evolution of the upper-level occupation probability P_+ , starting from the ground state (thick green curve) and the excited state (thin red curve). The inset shows the respective extended efficiency e , which is defined for each cycle as the difference of the probability at the beginning and the end of the small-energy-gap stage, shown by the yellow and black stars, respectively.

Results of calculations are further presented in Fig. S11 for (a) the incoherent ($\Omega < 2T_2^{-1}$) and (b) coherent ($\Omega \gtrsim 2T_2^{-1}$) cases. In Fig. S11(a) the red and green curves correspond to the resonant driving during either the high-energy stage or the low-energy stage, which describe the upper or lower panels in Fig. 1 of the main text, respectively. Thin dashed and dotted curves illustrate the situation of starting from a different initial condition, which is being in the excited state. Note that during the excitation, the system is first resonantly excited and then relaxes to the stationary solution, which makes a kink at the beginning of the “ON” stage. In Fig. S11(b), the numbers $n = 1, 2, 3$ denote the parameters, taken for the first three resonant points in Fig. 3(e) of the main text around $\delta\omega = 0$ and counted from the bottom. At long times, $t \gg T_{1,2}$, after the transient dynamics finishes, the upper-level occupation probability tends to its stationary solution P_+ . This is defined by the competition of excitation and relaxation, and is given by Eq. (S7), which gives $P_+ \leq 1/2$.

In Fig. S12 we present the calculated extended efficiency e , which is defined for each cycle as the difference of the probability at the beginning and the end of the small-energy-gap stage, see this in Fig. S11, shown by the arrows. Figure S12 is calculated for the incoherent regime, for the same parameters as Fig. S4. Note that for the stationary solution, the extended

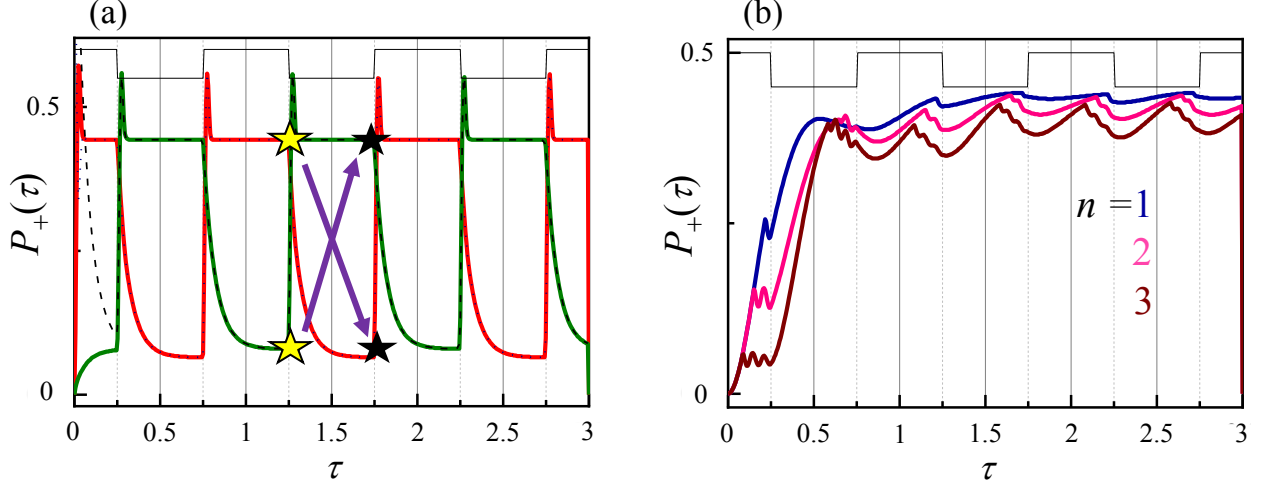


FIG. S11: Incoherent and coherent dynamics. The upper-level occupation probability P_+ is plotted as a function of the dimensionless time $\tau = \Omega t/2\pi$. Thin solid lines are given as a guide for the eye in order to mimic the large- and small-energy gap stages. The square modulation frequency $\Omega/2\pi$ is 0.2 MHz for (a) and 2 MHz for (b).

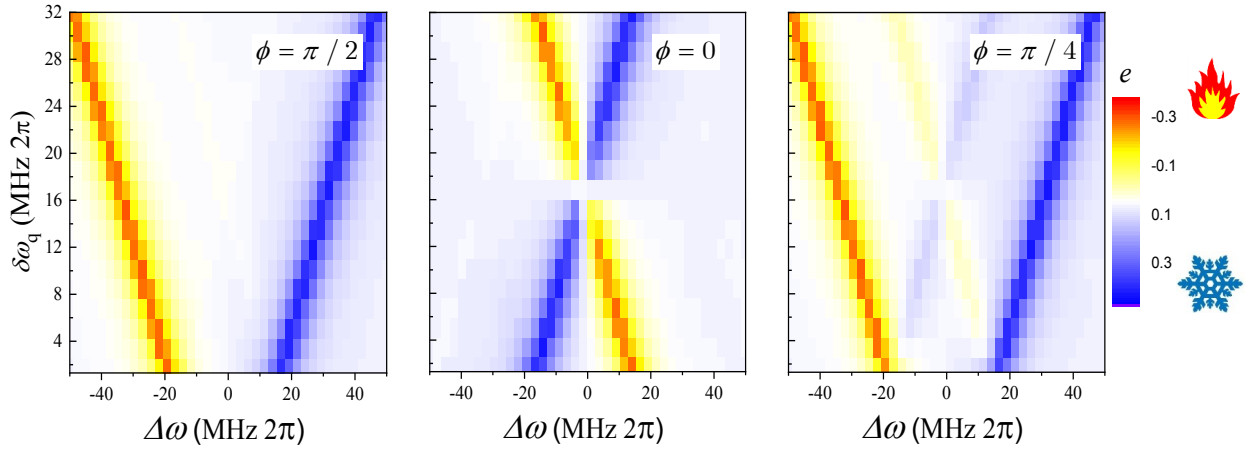


FIG. S12: Extended efficiency e in the incoherent regime. This is calculated for the same parameters as Fig. S4, as a function of the microwave frequency detuning $\Delta\omega = \omega_{\text{MW}} - \omega_q$ and the energy-level modulation amplitude $\delta\omega_q$.

efficiency e is close to 0 in the coherent regime (see Fig. 4 of the main text), while it displays both the heat-engine and refrigerator regimes in the incoherent regime, as shown in Fig. S12 by the red and blue colours, respectively.